Stability of the flow in a plane microchannel with one or two superhydrophobic walls

Jan O. Pralits, Edoardo Alinovi, and Alessandro Bottaro
DICCA, Scuola Politecnica University of Genova, 1 via Montallegro, 16145 Genova, Italy
(Received 5 July 2016; published 6 January 2017)

The modal and nonmodal linear stability of the flow in a microchannel with either one or both walls coated with a superhydrophobic material is studied. The topography of the bounding wall(s) has the shape of elongated microridges with arbitrary alignment with respect to the direction of the mean pressure gradient. The superhydrophobic walls are modeled using the Navier slip condition through a slip tensor, and the results depend parametrically on the slip length and orientation angle of the ridges. The stability analysis is carried out in the temporal framework; the modal analysis is performed by solving a generalized eigenvalue problem, and the nonmodal, optimal perturbation analysis is done with an adjoint optimization approach. We show theoretically and verify numerically that Squire's theorem does not apply in the present settings, despite the fact that Squire modes are found to be always damped. The most notable result is the appearance of a streamwise wall-vortex mode at very low Reynolds numbers when the ridges are sufficiently inclined with respect to the mean pressure gradient, in the case of a single superhydrophobic wall. When two walls are rendered water repellent, the exponential growth of the instability results from either a two-dimensional or a three-dimensional Orr-Sommerfeld mode, depending on the ridges' orientation and amplitude. Nonmodal results for either one or two superhydrophobic wall(s) display but a mild modification of the no-slip case.

DOI: 10.1103/PhysRevFluids.2.013901

I. INTRODUCTION

Superhydrophobic coatings represent an interesting technique for the possible reduction of drag in applications involving the flow of liquids over solid surfaces, for a wide range of Reynolds number, from laminar to turbulent conditions [1]. Such coatings work by the interposition of a gas layer between the liquid and the solid wall, trapped by distributed microscopic roughness elements present at the wall; over the gas layer the liquid can flow with negligible friction. Here we are concerned with the initial development stages of the laminar-turbulent transition for the flow of a liquid in a microchannel, with one or both walls characterized by a periodic, micropatterned topography.

Min and Kim [2] addressed this same hydrodynamic stability problem, considering isotropic, superhydrophobic channel walls (characterized, in an averaged sense, by the same scalar *slip length*, λ) and studied the case of both exponentially growing two-dimensional modes and three-dimensional pseudo-modes excited algebraically over short time intervals. Whereas two-dimensional Tollmien-Schlichting (TS) waves were stabilized by the use of a nonzero slip length, the effect of slip on the transient amplification of streaklike perturbations was found to be minor; Min and Kim performed also a few direct numerical simulations of transition to turbulence initiated by two-dimensional TS waves in different configurations (in the presence of only streamwise slip, only spanwise slip, or slip along both horizontal directions) finding that in some cases transition was advanced (with respect to the no-slip situation) and in others it was retarded. From the results it appears that it is the presence of spanwise slip (which is, in all practical cases, unavoidable when superhydrophobic surfaces are used) to favor the early triggering of transition.

Lauga and Cossu [3] also considered isotropic, superhydrophobic surfaces using a scalar slip length to model the wall. Their modal stability results demonstrated a strong stabilizing effect for two-dimensional TS waves (particularly when both channel walls display slip), whereas only a minor influence was found on the maximum transient energy growth of streamwise streaks.

Both of the studies cited above considered, appropriately, only a two-dimensional modal analysis on account of Squire's theorem; it will be demonstrated here that, under certain conditions not previously examined, three-dimensional modes can initiate the transition process when slip at the wall is present.

Very recently, Yu *et al.* [4] have reconsidered the temporal, modal stability problem for the flow in a channel with longitudinal superhydrophobic grooves on one or both walls, without employing the (averaging) concept of a slip length. They resolved the two-dimensional problem for the base flow in the plane orthogonal to the mean flow direction, and the two-dimensional problem for the disturbance field, assuming the interface flat and pinned at the corners of the ribs. When both the spanwise periodicity of the grooves and the shear-free fraction are sufficiently small, compared to the channel thickness, the results of the analysis by Yu *et al.* reproduce those obtained by employing a slip length. As the periodicity and the shear-free fraction are increased, a new wall mode is found, apparently related to the presence of inflection points in the mean, streamwise velocity profile; it is such a new mode which can lead the flow to an early instability. A similar conclusion as to the effect of the periodicity of the grooves has been reached by Luchini [5] who conducted direct numerical simulations of turbulence in a channel with two superhydrophobic walls, by comparing slip-length boundary condition cases with simulations carried out on walls with alternating no-slip and no-shear conditions (with the shear-free interface region of the same length as the no-slip region above the ribs). The conclusion by Luchini is that the concept of a slip length can be employed as long as the periodicity s^+ of the longitudinal microridges remains below about 30 (measured in wall units). To set ideas, let us see what the limit $s^+ = 30$ means for the practical case of a 20 m long planar object moving in water at 20 knots ($U \approx 10$ m/s). The momentum thickness θ varies from zero (at the leading edge of the body, where the boundary layer has not yet formed) to about 1.86 cm (near the trailing edge). The corresponding Re_θ thus reaches a value equal to about 1.86×10^5 at the end of the plate (where $\mathrm{Re}_x = 2 \times 10^8$), which translates into a friction coefficient $c_f = 2\tau_{\mathrm{wall}}/(\rho U^2)$ of approximately 1.5×10^{-3}. At the trailing edge of the plate ($x = 20$ m) the wall shear is about $\tau_{\mathrm{wall}} = 75$ Pa so that the friction velocity is $u_\tau = 0.274$ m s^{-1} and $s^+ = 30$ corresponds to a dimensional periodicity s of about 100 μm. This latter value is close to being an upper bound of the characteristic length scales of superhydrophobic surfaces.

Note, incidentally, that a value of s^+ of about 15 provides optimal drag reducing properties for the case of longitudinal riblets [6–8], while for s^+ exceeding 30 skin friction drag is generally increased with respect to the base value. It is advantageous, for superhydrophobic drag reduction purposes, to have the periodicity s of the microridges as large as possible, with a large gas fraction exposed to water. The value $s^+ = 30$ yields dimensional values of periodicity of the order of 100 μm (cf. arguments given above), which might be used in practice to prevent the escape, and limit the diffusion into water, of the gas bubbles. The limit imposed on s^+ justifies the use of simplified simulations with homogeneous Navier slip conditions.

A practical limitation on the effectiveness of superhydrophobic surfaces lies in the possible wetting of the surface because of surface defects, or because of the effect of large liquid pressure or diffusion of the gas into the liquid. Furthermore, in the case of parallel microgrooves such as those studied here, the gas plastron may be washed out by the shearing action of the liquid above. Some remedies against the loss of the slip effect have been provided in recent years. In particular, it has been suggested to nanostructure the sidewalls of the microstructures [9] or to pressurize the gas layer [10], but these measures are ineffective once the gas layer is disrupted. Restoration of the gas plastron after wetting can, however, be achieved by nanostructuring the bottom surface of the ridges and electrolytically generating new gas [11]. We finally observe that longitudinal microridges or microgrooves of periodicity s^+ equal to about 15 could be used advantageously also in the case where the *wetting transition* [12] takes place, by exploiting the "riblet effect."

The surface topography is rendered in the present work by a Navier slip condition [13,14], which represents, in an homogenized sense, the alternation of no-slip and no-shear elongated regions which are found when microridges cover the walls, under the assumption that the gas in the cavities exerts no shear stress on the liquid above it. For a comparison between different surface structures the

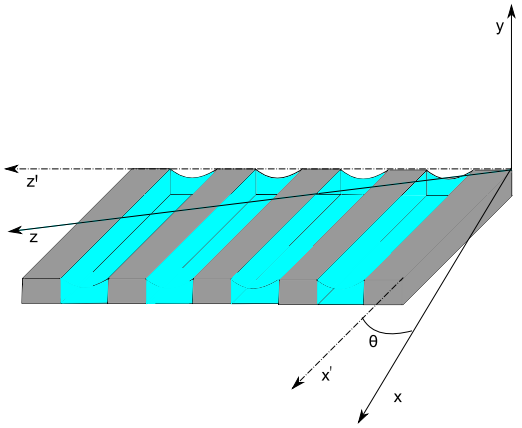

FIG. 1. Sketch of the wall pattern with definition of axes, angle θ, and ridges periodicity s. The gas-liquid interface is represented as a curved surface in light blue (gray) color for illustrative purposes; the way in which the Navier slip lengths are modified by the curvature of the interface has been addressed by Teo and Khoo [18].

reader is referred to Bottaro [1]; see in particular Fig. 10 there, showing that the effective slip length is of the order of the pattern periodicity, and decreasing with the solid area fraction. In the present paper linear stability results are obtained for both modal and nonmodal amplification of disturbances, for microridges aligned, orthogonal, or at an angle, to the driving pressure gradient. In view of the recent paper by Yu *et al.* [4] it is clear that the results presented here apply only when s is sufficiently small.

II. PROBLEM FORMULATION

The effect of superhydrophobic (SH) surfaces on the instability onset, and consequently the initial stages of laminar-turbulent transition, is addressed in the framework of plane microchannels where the Reynolds number is typically small. We assume that the channel has thickness $2h^\star$ and use $h^\star$ to normalize distances, and the bulk speed $\bar{U}^\star$ is employed to scale the velocity. The superscript $\star$ denotes dimensional quantities. The SH riblet-like wall considered here forms an anisotropic texture (Fig. 1) for which a slip tensor $\mathbf{\Lambda}$ in the plane of the walls (x,z) can be defined [15–17] as

$$\mathbf{\Lambda} = \mathbf{Q}\begin{bmatrix}\lambda^{\parallel} & 0\\ 0 & \lambda^{\perp}\end{bmatrix}\mathbf{Q}^T, \quad \text{with} \quad \mathbf{Q} = \begin{bmatrix}\cos\theta & -\sin\theta\\ \sin\theta & \cos\theta\end{bmatrix}, \tag{1}$$

where $\lambda^{\parallel}$ and $\lambda^{\perp}$ are the eigenvalues of the slip tensor $\mathbf{\Lambda}$ for $\theta = 0,90^\circ$, and the transformation (1) represents a rotation of the tensor by an angle θ. For $\theta = 0^\circ$ the ridges are aligned with x, and for $\theta = 90^\circ$ they are aligned with z. In the special case of isotropic SH it is $\lambda^{\parallel} = \lambda^{\perp}$; for the case of microridges aligned along the mean pressure gradient [13,14,17] we have $\lambda^{\parallel} = 2\lambda^{\perp}$. This latter result will be used hereafter, and the results will be expressed as a function only of $\lambda^{\parallel}$.

By denoting with u,v and w the streamwise, wall-normal, and spanwise velocity components, respectively, the dimensionless boundary conditions for the horizontal velocity components at the two walls in $y = \pm 1$ read

$$\begin{bmatrix}u(x,-1,z)\\ w(x,-1,z)\end{bmatrix} = \mathbf{\Lambda}\frac{\partial}{\partial y}\begin{bmatrix}u(x,-1,z)\\ w(x,-1,z)\end{bmatrix}, \tag{2}$$

$$\begin{bmatrix}u(x,1,z)\\ w(x,1,z)\end{bmatrix} = -\mathbf{\Lambda}\frac{\partial}{\partial y}\begin{bmatrix}u(x,1,z)\\ w(x,1,z)\end{bmatrix}, \tag{3}$$

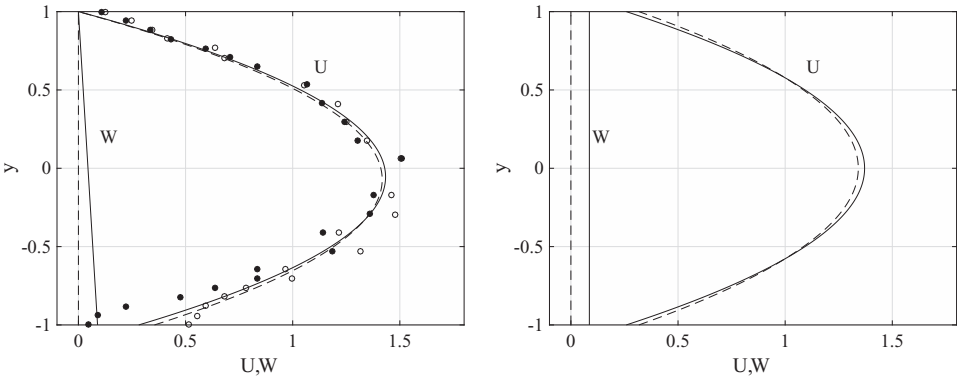

FIG. 2. Streamwise U and spanwise W velocity components of the base flow when $\lambda^{\parallel} = 0.155$ for the cases $\theta = 0^{\circ}$ (dashed) and $\theta = 45^{\circ}$ (solid). Left: one superhydrophobic wall. Right: two superhydrophobic walls. The symbols show the experimental micro-PIV data of Ref. [20]; the filled circles show measurements above the ribs, whereas the empty symbols are taken above the gas-water interface.

in the case of both walls being textured, plus vanishing conditions for the vertical velocity component v at the two walls. If one of the two walls is not superhydrophobic, the condition there is simply $\mathbf{u} = \mathbf{0}$.

A. Base flow and linear stability equations

The velocity and pressure are decomposed into a steady base flow and an unsteady disturbance according to

$$\mathbf{u}(x,y,z,t) = \mathbf{U}(x,y,z) + \epsilon \mathbf{u}'(x,y,z,t), \quad p(x,y,z,t) = P(x,y,z) + \epsilon p'(x,y,z,t), \tag{4}$$

with $\epsilon \ll 1$. The governing equations for plane, incompressible, and steady channel flow read

$$\frac{dP}{dx} = \frac{1}{\mathrm{Re}} \frac{d^2U}{dy^2}, \quad V = 0, \quad \frac{d^2W}{dy^2} = 0, \tag{5}$$

where the Reynolds number is defined as $\mathrm{Re} = \bar{U}^{\star} h^{\star}/\nu^{\star}$. When the boundary conditions (2)–(3) are used, the analytical solution of the base flow, in the case of two superhydrophobic walls, reads

$$U(y) = -3\frac{y^2 - 1 - \lambda^{\parallel}(1 + \cos^2\theta)}{2 + 3\lambda^{\parallel}(1 + \cos^2\theta)}, \quad W(y) = 3\frac{\lambda^{\parallel} \sin\theta \cos\theta}{2 + 3\lambda^{\parallel}(1 + \cos^2\theta)}. \tag{6}$$

When θ differs from 0° and 90°, a small component of the base flow orthogonal to the mean pressure gradient is created in the channel [19]. In the case in which only the bottom wall is superhydrophobic the basic flow is

$$U(y) = -\frac{3}{4}\frac{(y^2 - 1)(8 + 6\lambda^{\parallel} + {\lambda^{\parallel}}^2) + 2\lambda^{\parallel}(y - 1)(2 + 2\cos^2\theta + \lambda^{\parallel})}{6\lambda^{\parallel} + 3\lambda^{\parallel}\cos^2\theta + 4 + 2{\lambda^{\parallel}}^2}, \tag{7}$$

$$W(y) = -3\lambda^{\parallel}\frac{\sin\theta\cos\theta(y - 1)(4 - \lambda^{\parallel}\cos^2\theta + 2\lambda^{\parallel})}{[4 + \lambda^{\parallel}(1 + \sin^2\theta)](6\lambda^{\parallel} + 3\lambda^{\parallel}\cos^2\theta + 4 + 2{\lambda^{\parallel}}^2)}, \tag{8}$$

and this flow presents a streamwise component of the vorticity which is maximized by $\theta = \pm 45^{\circ}$ when $\lambda^{\parallel}$ is smaller than about 0.1 (above this value of $\lambda^{\parallel}$ the absolute value of the inclination angle of the grooves which display the largest vorticity increases mildly). Examples of the base flow for $\lambda^{\parallel} = 0.155$, in the case of one and two superhydrophobic walls, are displayed in Fig. 2 for two values of θ.

The linear stability equations are obtained by introducing (4) into the Navier-Stokes equations and collecting terms of order ϵ. In primitive variable form they read

$$\frac{\partial u'}{\partial x} + \frac{\partial v'}{\partial y} + \frac{\partial w'}{\partial z} = 0, \tag{9}$$

$$\frac{\partial u'}{\partial t} + U\frac{\partial u'}{\partial x} + v'\frac{dU}{dy} + W\frac{\partial u'}{\partial z} = -\frac{\partial p'}{\partial x} + \frac{1}{\mathrm{Re}}\nabla^2 u', \tag{10}$$

$$\frac{\partial v'}{\partial t} + U\frac{\partial v'}{\partial x} + W\frac{\partial v'}{\partial z} = -\frac{\partial p'}{\partial y} + \frac{1}{\mathrm{Re}}\nabla^2 v', \tag{11}$$

$$\frac{\partial w'}{\partial t} + U\frac{\partial w'}{\partial x} + v'\frac{dW}{dy} + W\frac{\partial w'}{\partial z} = -\frac{\partial p'}{\partial z} + \frac{1}{\mathrm{Re}}\nabla^2 w', \tag{12}$$

with $\nabla^2 = \frac{\partial^2}{\partial x^2} + \frac{\partial^2}{\partial y^2} + \frac{\partial^2}{\partial z^2}$. The disturbance field (denoted by primes) is expressed in terms of Fourier modes along the wall-parallel directions,

$$q'(x,y,z,t) = \tilde{q}(y,t)\exp[i(\alpha\, x + \beta\, z)] + \text{c.c.}, \tag{13}$$

for the generic variable q', where α and β are the streamwise and spanwise wave numbers, respectively, and c.c. denotes complex conjugate. The governing linear equations (9)–(12) are supplemented by the boundary conditions (2) and (3) for the disturbance variables in the case of two superhydrophobic walls. In the case of one SH wall, the other wall is given a no-slip condition, $\mathbf{u}' = \mathbf{0}$. The theory developed is applicable as long as the disturbance wavelength $2\pi/k$, with $k = \sqrt{\alpha^2 + \beta^2}$, is sufficiently longer than the spatial periodicity s of the microridges.

B. Modal analysis

The modal analysis is performed by assuming a temporal behavior of the form

$$\tilde{q}(y,t) = \hat{q}(y)\exp(-i\,\omega\, t), \tag{14}$$

where $\omega = \omega_r + i\omega_i$ is the complex angular frequency (subscript i denotes imaginary part, subscript r denotes real part) and $\omega_i > 0$ indicates unstable solutions. Substituting the asymptotic temporal behavior (14) into the linearized equations (9)–(12) yields a generalized eigenvalue problem. In discrete form the resulting system of equations can be written as

$$i\omega\mathbf{B}\hat{\mathbf{q}} = \mathbf{A}\hat{\mathbf{q}}, \tag{15}$$

where $\hat{\mathbf{q}} = (\hat{u},\hat{v},\hat{w},\hat{p})$; $\mathbf{A}$ and $\mathbf{B}$ are complex-valued $4n \times 4n$ matrices, and n is the number of discrete points taken in the y direction. In a channel with no-slip walls, Squire's theorem states that the instability of the coupled system stems from the amplification of a two-dimensional Orr-Sommerfeld mode [21]. This is proven by applying Squire's transformation ($k\,u_{2D} = \alpha\hat{u} + \beta\hat{w}$; $k\,\mathrm{Re}_{2D} = \alpha\,\mathrm{Re}$; $p_{2D}/k = \hat{p}/\alpha$; $v_{2D} = \hat{v}$; $\omega_{2D}/k = \omega/\alpha$) to the linearized system. The result is that, if a three-dimensional mode is unstable, a two-dimensional mode will be unstable at a lower value of the Reynolds number, $\mathrm{Re}_{2D} = \alpha\,\mathrm{Re}/k \leqslant \mathrm{Re}$. Furthermore, it can be shown, always in the no-slip case, that Squire modes (eigensolutions of the unforced Squire's equation for the vertical vorticity component) are always damped. In the present wall-slip case, however, the statements above do not necessarily apply.

1. A digression on Squire's theorem and Squire modes

By decomposing the velocity vector $\hat{\mathbf{u}} = (\hat{u},\hat{v},\hat{w})$ into components parallel and perpendicular to the wave number vector,

$$u_{\parallel} = \frac{(\alpha\hat{u} + \beta\hat{w})}{k}, \quad u_{\perp} = \frac{(\beta\hat{u} - \alpha\hat{w})}{k},$$

the governing equations satisfied by $(u_\parallel, v_{2D}, p_{2D})$ are independent of $u_\perp$:

$$iku_\parallel + \frac{dv_{2D}}{dy} = 0, \tag{16}$$

$$-i\omega_{2D}u_\parallel + ik\overline{U}u_\parallel + \frac{d\overline{U}}{dy}v_{2D} = -ikp_{2D} + \frac{1}{\mathrm{Re}_{2D}}\left(\frac{d^2}{dy^2} - k^2\right)u_\parallel, \tag{17}$$

$$-i\omega_{2D}v_{2D} + ik\overline{U}v_{2D} = -\frac{dp_{2D}}{dy} + \frac{1}{\mathrm{Re}_{2D}}\left(\frac{d^2}{dy^2} - k^2\right)v_{2D}. \tag{18}$$

Whereas at first sight this appears to imply that Squire's theorem is satisfied, it is not the case, since (1) the base flow of this new two-dimensional problem is different from U (it is $\overline{U} = U + \frac{\beta}{\alpha}W$) and (2) the boundary conditions for the parallel component do not decouple, i.e., at $y = \pm 1$ the boundary conditions are expressed in terms of both $u_\parallel$ and $u_\perp$. The decoupling of the problem into two separate problems (a homogeneous problem for $(u_\parallel, v_{2D}, p_{2D})$ and a second problem for $u_\perp$, forced by v_{2D}) is possible only in the case of isotropic SH walls (i.e., $\lambda_\parallel = \lambda_\perp$ and $W = 0$), and it is only in this case that Squire's theorem holds.

Furthermore, the fact that Squire modes are not necessarily damped can be seen by considering the equation for the velocity component perpendicular to the wave vector,

$$\left[-i\omega + i\alpha U + i\beta W - \frac{1}{\mathrm{Re}}\left(\frac{d^2}{dy^2} - k^2\right)\right]u_\perp = \left(\beta\frac{dU}{dy} - \alpha\frac{dW}{dy}\right)\frac{v_{2D}}{k}, \tag{19}$$

known as Squire's equation. By multiplying the homogeneous equation (19) by $u_\perp^*$, with the $*$ superscript denoting complex conjugate, and integrating in y across the fluid domain, we have

$$\omega\int_{-1}^{1} u_\perp^* u_\perp \, dy = \int_{-1}^{1}\left[(\alpha U + \beta W)u_\perp^* u_\perp + \frac{i}{\mathrm{Re}}u_\perp^*\left(\frac{d^2}{dy^2} - k^2\right)u_\perp\right] dy. \tag{20}$$

Integrating by parts once and taking the imaginary part it is found

$$\omega_i\int_{-1}^{1}|u_\perp|^2\, dy = -\frac{1}{\mathrm{Re}}\int_{-1}^{1}\left(\left|\frac{du_\perp}{dy}\right|^2 + k^2|u_\perp|^2\right) dy + \frac{A}{\mathrm{Re}}, \tag{21}$$

with

$$A = \frac{1}{k^2}\left[\alpha^2\left(\hat{w}_r\frac{d\hat{w}_i}{dy} - \hat{w}_i\frac{d\hat{w}_r}{dy}\right) + \beta^2\left(\hat{u}_r\frac{d\hat{u}_i}{dy} - \hat{u}_i\frac{d\hat{u}_r}{dy}\right)\right.$$
$$\left. + \alpha\beta\left(\hat{u}_i\frac{d\hat{w}_r}{dy} + \hat{w}_i\frac{d\hat{u}_r}{dy} - \hat{u}_r\frac{d\hat{w}_i}{dy} - \hat{w}_r\frac{d\hat{u}_i}{dy}\right)\right]_{-1}^{1}. \tag{22}$$

There is no evident reason why A, which contains boundary terms arising from integration by parts, should be negative [or positive and small, so as not to render positive the right-hand-side of Eq. (21)]; thus, Squire modes (characterized by $\hat{v} \equiv 0$ throughout y) can, in principle, be amplified [since ω_i in Eq. (21) is not necessarily negative].

In our experience, however, Squire modes remain damped (cf. Sec. III), both those in the so-called A branch (also known as *wall modes*) and those in the P branch (*center modes*). Conversely, recent results by Szumbarski [22] and Mohammadi *et al.* [23] for the flow in channels with streamwise-invariant and spanwise-periodic corrugations demonstrate that it is precisely the least stable Squire mode (in the P branch) which can become unstable for a sufficiently large corrugation amplitude. When the amplitude of the corrugation exceeds a value of $O(10^{-2})$ an inviscid mechanism, driven by the spanwise gradient of the main velocity component, forces the destabilization of the Squire *center* mode. These findings are related to those by Yu *et al.* [4], who focused, however, on *wall* modes. We reemphasize that the rough walls considered have spatial scales sufficiently small for an homogenisation procedure, leading to the Navier-slip concept, to be tenable.

C. Nonmodal analysis

The nonmodal behavior is studied by computing the maximum finite-time amplification; the initial disturbance velocity field, $\tilde{\mathbf{u}}_0$, is *optimal* when the gain

$$G(\mathrm{Re},\alpha,\beta,T,\lambda^{\parallel},\theta) = \frac{e(T)}{e(0)} \tag{23}$$

is maximized, where

$$e(t) = \frac{1}{2}\int_{-1}^{1} (\tilde{u}\tilde{u}^* + \tilde{v}\tilde{v}^* + \tilde{w}\tilde{w}^*)\, dy,$$

and T is the target time of the optimization. This is conducted by introducing Lagrange multipliers enforcing the constraints given by the governing linear equations and the boundary conditions. The corresponding adjoint equations are derived using a discrete approach [24]. We further define

$$G_M(\mathrm{Re},\lambda^{\parallel},\theta) = \max_{\forall\alpha,\beta,T} G,$$

when G is maximized with respect to the wave numbers (α,β) and the final time T. The final time and spanwise wave number corresponding to G_M are denoted T_M and β_M, respectively.

D. Numerical procedure

The equations are written in primitive variable form and discretized on a staggered grid. The spatial derivatives are discretized using second order finite differences and a semi-implicit second-order scheme is used to advance in time. A uniform grid is adopted along the y direction, and 300 discrete points are sufficient to obtain converged eigenvalues, with errors with respect to reference solutions lower than 0.1%. The code used to compute the nonmodal growth has been tested on several cases found in the literature (using no-slip boundary conditions); in particular, the value of the optimal gain $G_M = 2\times10^{-4}\,\mathrm{Re}^2$ and the corresponding time at which it is achieved, $T_M = 0.076\,\mathrm{Re}$, with $\alpha = 0$ and $\beta = 2.04$, are recovered within less than 0.1% [21]. Results are obtained imposing that convergence is reached when the relative difference in gain between two consecutive iterations is below 10^{-8}.

III. RESULTS

The instability onset, in the case of modal growth, and the largest temporal amplification, in the case of nonmodal growth, are studied parametrically for both one and two SH channel walls.

A. Modal analysis

We initiate the discussion of the modal results by showing some representative behaviors for the case of a single superhydrophobic wall. Figure 3 (top, left) illustrates the variation of the growth rate ω_i of the most unstable (or least stable) Orr-Sommerfeld (OS) mode as a function of the slip length, for the parameters indicated in the figure's caption. The wave angle considered is $\Phi = \tan^{-1}\beta/\alpha = 20^\circ$; this three-dimensional mode is initially damped at low $\lambda^{\parallel}$. However, past a threshold value of the slip length, the mode becomes unstable with a maximum growth rate which is achieved at $\lambda^{\parallel} = 0.25$. The disturbance mode shapes in correspondence to this point are plotted in the left frame, center row, of Fig. 3; they correspond to classical OS eigenfunctions, asymmetric about $y = 0$ because of the slip condition at $y = -1$. On the right side of Fig. 3 the behavior of a different mode is represented, at a much smaller value of the Reynolds number than the one considered so far. This instability mode displays a comparable behavior of the growth rate as a function of $\lambda^{\parallel}$ (an initial decrease of ω_i, followed by an increase, with a maximum amplification for $\lambda^{\parallel} = 0.145$), but radically different eigenfunctions, displayed in the center row, right frame.

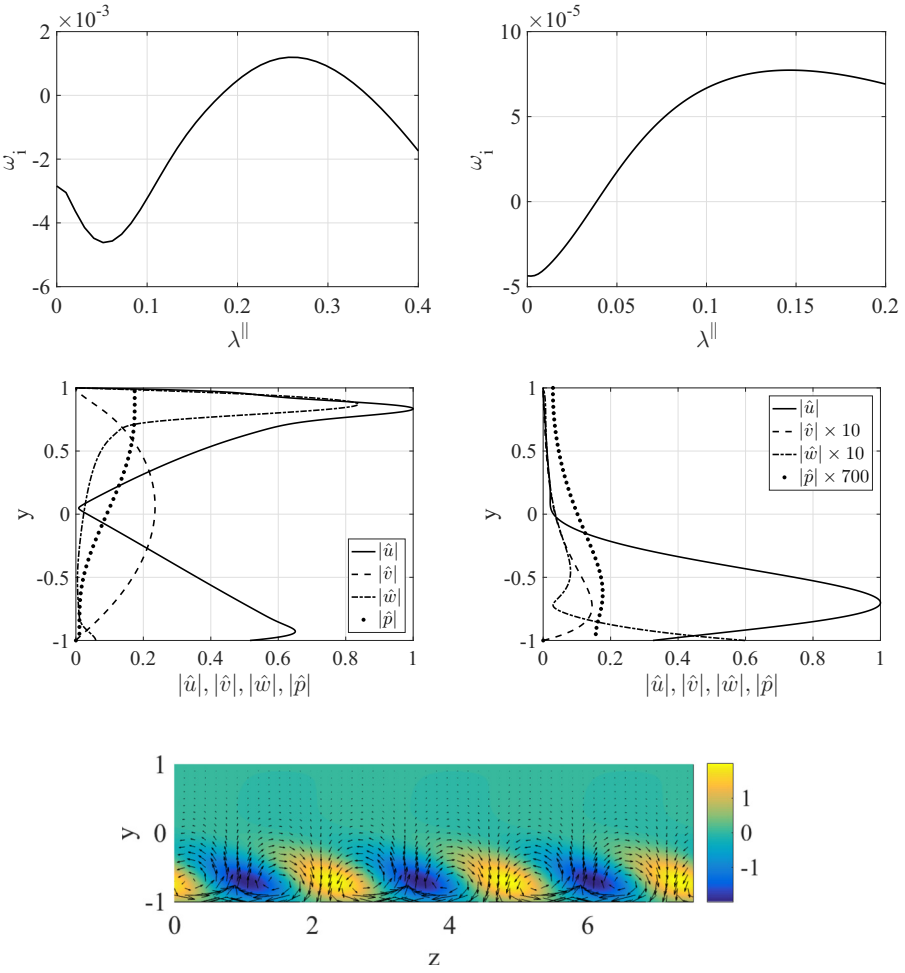

FIG. 3. Growth rate ω_i as a function of $\lambda^{\parallel}$ (top), and absolute value of the disturbance velocity components (u,v,w) and disturbance pressure (middle) normalized by the maximum value of the streamwise component, using one SH wall. With reference to the four top frames, in the left column the parameters are $\mathrm{Re} = 10\,000$, $\theta = 80^\circ$, $\Phi = 20^\circ$, and $\alpha = 0.65$, whereas in the right column we have $\mathrm{Re} = 2000$, $\theta = 45^\circ$, $\Phi \approx 90^\circ$, and $\alpha \approx 0$. The values of $\lambda^{\parallel}$ in the middle row, where eigenfunctions are plotted, correspond to the maximum growth rate for the respective case (0.25,0.145). In the bottom row, vectors and contours, in the (y,z) plane, of the velocity components relative to the case in the right column are shown over three spanwise periods ($\beta = 2.5$). The shaded contours represent the positive and negative streamwise disturbance velocity component, whereas the vectors represent wall-normal and spanwise components.

This mode, which is found to be dominating when the ridges are at an angle around 45° to the mean pressure gradient, takes the form of near-wall vortices, as exemplified on the bottom frame of Fig. 3. Alternating high and low speed streaks, elongated in the streamwise direction x ($\alpha = 10^{-3}$ in all the calculations where we write $\alpha \approx 0$, the case α exactly equal to zero being ill-posed numerically), are present near the SH wall, with corresponding low-amplitude secondary vortices. While it is not a surprise that inclined ridges at the wall yield low-frequency streamwise or quasistreamwise vortices, it is remarkable that this behavior is rendered so clearly by the homogenized Navier-slip boundary condition. This new instability mode depends crucially on the wall ridges' amplitude (a threshold value, $\lambda^{\parallel} = 0.038$, is found with the present settings) and orientation with respect to the

mean pressure gradient, i.e., θ, and displays a temporal amplification factor typically larger than the most unstable three-dimensional OS wave for the same value of Re.

It is now instructive to examine the spectra, in terms of either the complex phase speed c or the complex frequency ω, depending on the value of the streamwise wave number, for the two cases discussed so far; such spectra are plotted in Fig. 4. The figure on the top is the classical spectrum which can be observed when α is not close to zero, with the three branches, classically denoted as A, P, and S; this figure displays, in fact, all of the eigenvalues which appear when $\lambda^{\parallel}$ varies in the range [0,0.4]. It is interesting to observe that the degenerate Squire modes of branch A [shown with red (gray) bullets] split: such degenerate modes correspond, in the no-slip case, to a symmetric-antisymmetric couple of $\hat{u}$ eigenfunctions. When slip occurs on one wall, one of the two wall modes of the initially degenerate pair in branch A moves rapidly away from the $\lambda^{\parallel} = 0$ value, thus displaying a very strong sensitivity (in fact, also OS wall modes are highly sensitive). Despite this, the Squire eigenvalues, both the wall modes and the center modes, never cross the real axis in all cases considered here, and the mode which becomes unstable is the three-dimensional OS mode with c_r close to 0.2. The picture is radically different for the case of ridges at 45° to the mean pressure gradient (bottom frame); as $\lambda^{\parallel}$ increases, the modes which are initially degenerate, all damped and concentrated along a single vertical line with $\omega_r \approx 0$ (for $\lambda^{\parallel} = 0$), separate and diverge from one another. The continuous line in the bottom frame joins all the least stable modes found for $\lambda^{\parallel} < 0.038$ and the unstable modes which exist when $\lambda^{\parallel}$ exceeds 0.038.

The results obtained so far indicate that a new wall-vortex mode, driven by the presence of inclined wall ridges of sufficiently large amplitude, exists when Re is rather small, to presumably dominate the early stages of the transition process. A parametric study, with θ and $\lambda^{\parallel}$ varied systematically to infer trends, is reported in Figs. 5 and 6. The first of these figures show that the OS mode identifies the critical conditions only when θ is close to 0° and 90°; for θ in a range around 45° (a range which is wider with the increase of $\lambda^{\parallel}$) the wall-vortex mode is the dominating instability. The smallest critical Reynolds numbers, Re_c, are found at 45° for both cases examined in Fig. 5 and are around a value of 1000, much smaller than the values of the corresponding neutral OS modes. The critical wave angle is 90° in the range of θ where this new instability dominates. Figure 6 shows the behavior of the most unstable, two-dimensional OS mode (solid lines) which leads the instability when $\theta = 0°$, and the switch between the OS wave and the wall-vortex mode, when $\theta = 45°$, taking place at $\lambda^{\parallel} = 0.033$. As expected from previous studies, a stabilization effect (i.e., an increase of Re_c) is found for the OS mode as $\lambda^{\parallel}$ grows from zero ($\mathrm{Re}_c = 3848$ for $\lambda^{\parallel} = 0$). However, when the ridges are at an angle of 45° the OS mode is eventually overruled by the streamwise wall-vortex mode, which becomes unstable at progressively smaller values of the Reynolds number; for $\lambda^{\parallel}$ above a value approximately equal to 0.15 an asymptotic value of the critical Re close to 600 is reached for the onset of the wall-vortex mode.

The case of two superhydrophobic walls is considered next where we report results both for low values of $\lambda^{\parallel}$ as well as those used in Figs. 5 and 6 concerning a single SH wall. The reason for considering also lower values of $\lambda^{\parallel}$ stems from the knowledge [1] that, when the walls are isotropic, a comparable stabilizing effect is achieved in the case of two SH walls for a value of the slip length ten times smaller than for a single SH wall. The results are summarized by Figs. 7 and 8. The notable effect in this case is that the streamwise wall-vortex mode does not emerge, with a competition which is now established between two-dimensional and three-dimensional OS modes; Fig. 7 shows that the onset of an exponential instability is delayed when $\lambda^{\parallel}$ is increased and that the two-dimensional OS wave (with $\Phi_c = 0$) dominates the transition process only for θ sufficiently large (the switch-over value increasing with $\lambda^{\parallel}$). The stabilizing effect of $\lambda^{\parallel}$ is confirmed by Fig. 8; for $\lambda^{\parallel}$ below 0.01 the stability characteristics are similar to those of the no-slip case, and two-dimensional OS modes prevail (for any value of θ). In the case of ridges inclined at an angle of 45° to the mean streamwise velocity component, the mode which takes the lead past $\lambda^{\parallel} = 0.033$ is quasistreamwise (α is small and decreasing). With increasing values of $\lambda^{\parallel}$ (0.07 and 0.155) the values of the critical Reynolds numbers are increased for small enough and large enough ridge angles. For intermediate values of the ridge angle no instability delay (increased critical Reynolds number) is obtained for $\lambda^{\parallel} > 0.05$.

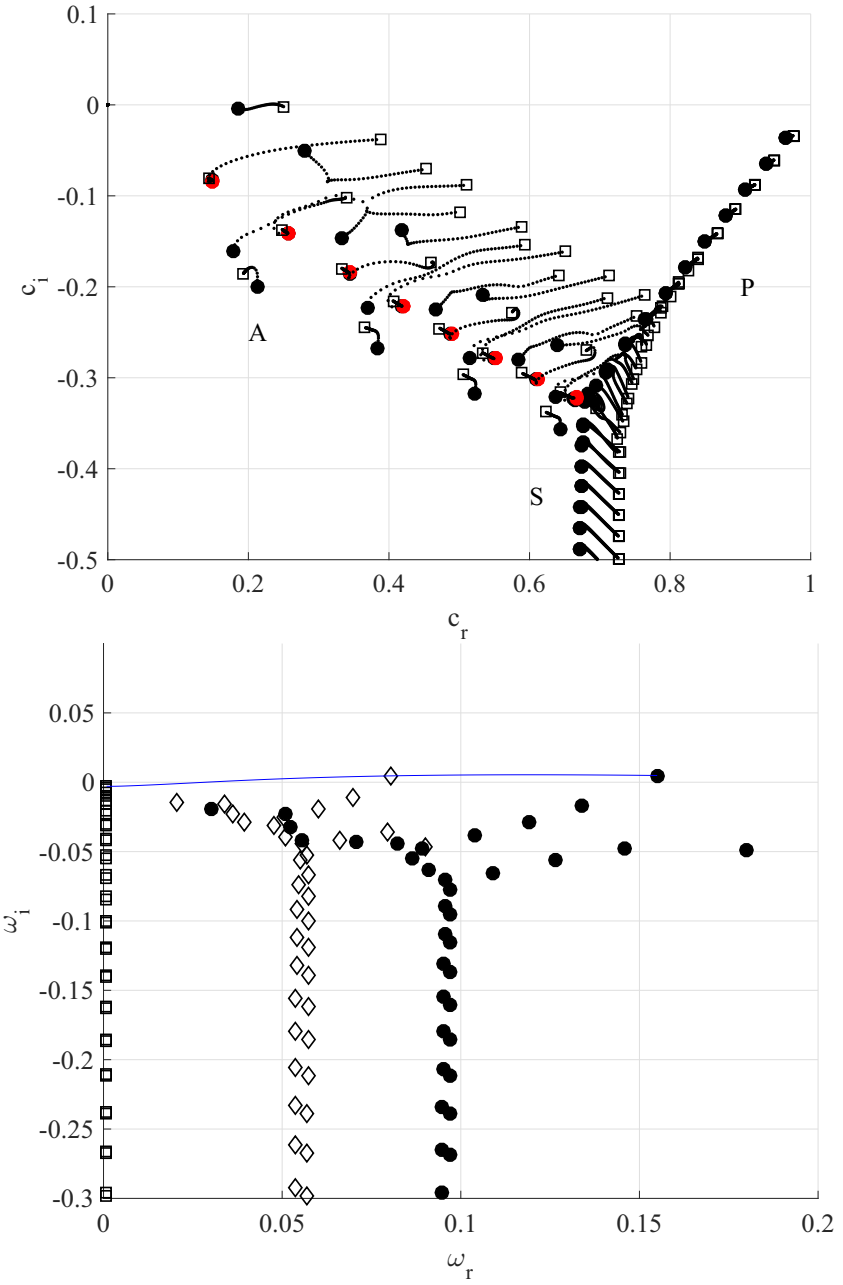

FIG. 4. (Top) Spectra of the complex phase velocity c in the case of one SH wall when $\mathrm{Re} = 10\,000$, $\theta = 80^\circ$, $\Phi = 20^\circ$, and $\alpha = 0.65$ and different values of $\lambda^\parallel$. The filled circles correspond to $\lambda^\parallel = 0$; in particular, the red (gray) bullets show the Squire modes on branch A. The open squares represent the spectrum for $\lambda^\parallel = 0.4$, and the dots show the trajectory of each eigenmode when $\lambda^\parallel$ varies from 0 to 0.4. (Bottom) Spectra of the complex frequency ω in the case of one SH wall when $\mathrm{Re} = 2000$, $\theta = 45^\circ$, $\Phi = 89.98^\circ$, and $\alpha = 0.001$. The open squares, diamonds and filled circles show the spectra for $\lambda^\parallel = 0,\ 0.1,\ 0.2$, respectively. The continuous line traces the least stable (or the most unstable) mode for $\lambda^\parallel$ varying in the range [0,0.2].

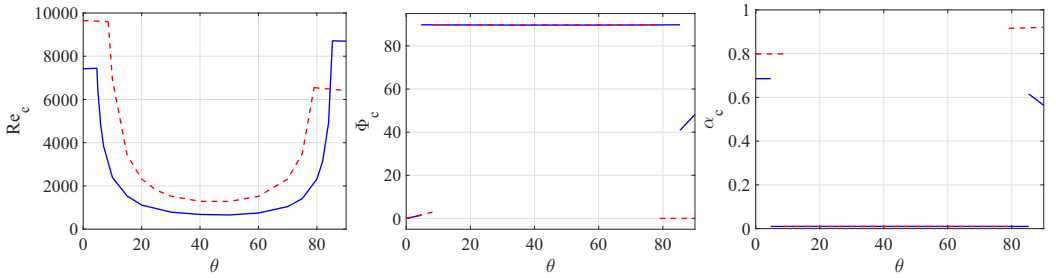

FIG. 5. Critical Reynolds number Re_c (left), the corresponding wave angle (middle) and streamwise wave number (right) as a function of θ for the case of $\lambda^{\parallel} = 0.07$ (dashed line) and $\lambda^{\parallel} = 0.155$ (solid line) for one SH wall.

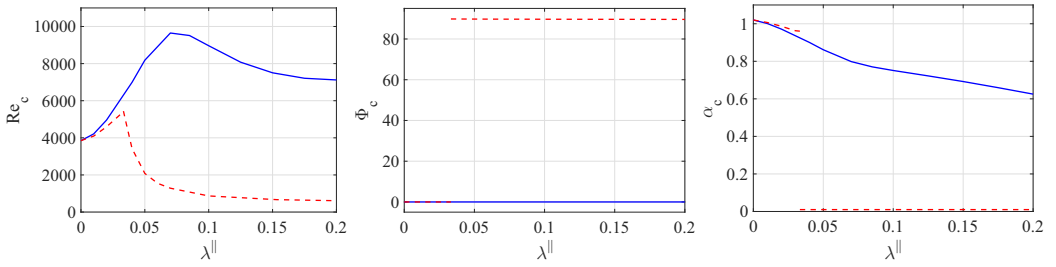

FIG. 6. Critical Reynolds number Re_c (left), the corresponding wave angle (middle), and corresponding streamwise wave number (right) as a function of $\lambda^{\parallel}$ for the case of $\theta = 0^{\circ}$ (solid line) and $\theta = 45^{\circ}$ (dashed line) in the presence of one SH wall.

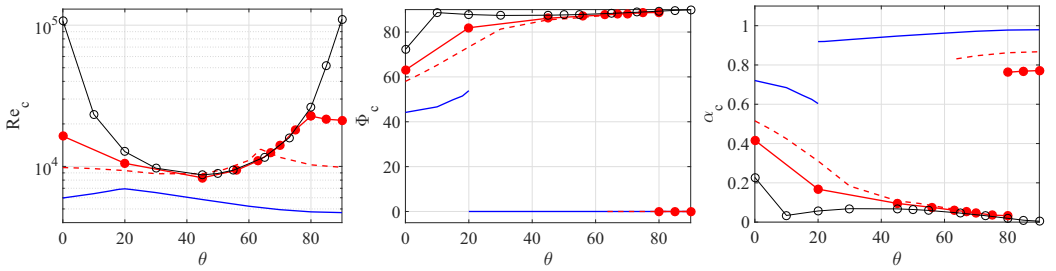

FIG. 7. Critical Reynolds number Re_c (left) and corresponding wave angle (middle) and streamwise wave number (right) as a function of θ for the case of $\lambda^{\parallel} = 0.02$ (solid line), $\lambda^{\parallel} = 0.05$ (dashed line), $\lambda^{\parallel} = 0.07$ (solid line with filled circles), $\lambda^{\parallel} = 0.155$ (solid line with open circles) in the presence of two SH walls.

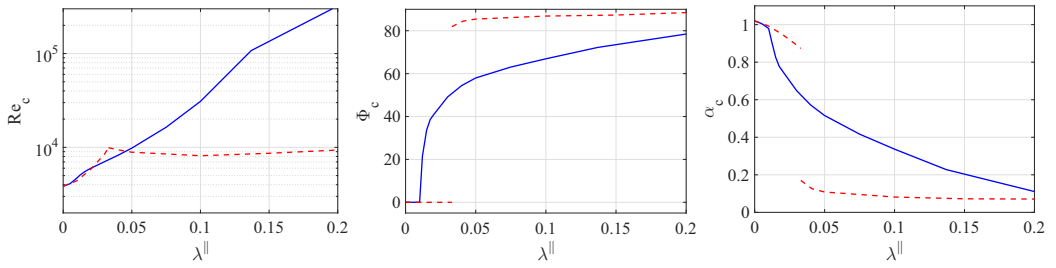

FIG. 8. Critical Reynolds number Re_c (left) and corresponding wave angle (middle) and streamwise wave number (right) as a function of $\lambda^{\parallel}$ for the case of $\theta = 0^{\circ}$ (solid line) and $\theta = 45^{\circ}$ (dashed line) in the presence of two SH walls.

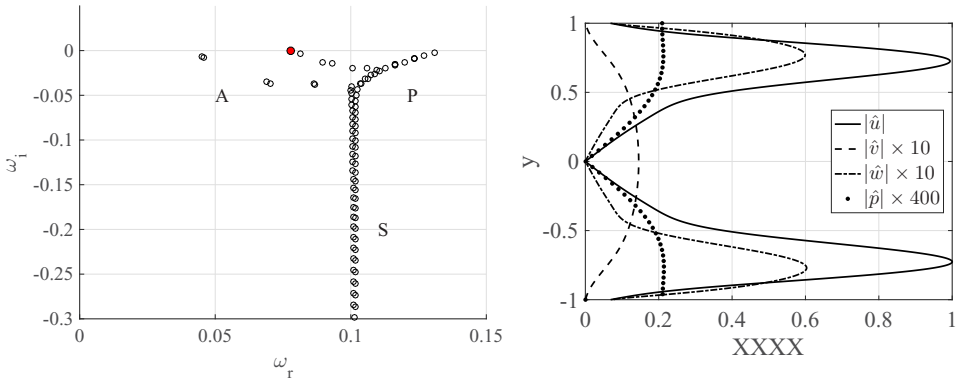

FIG. 9. Spectra of the complex frequency ω, with the unstable mode marked with a red (gray) bullet (left), absolute value of the disturbance velocity components (u,v,w), and disturbance pressure of the unstable mode (right), for Re $= 10\,000$, $\lambda^{\parallel} = 0.05$, $\theta = 45^{\circ}$, $\alpha = 0.1$, $\Phi = 86^{\circ}$ ($\beta = 1.4$).

This asymptotic behavior is observed also against variations in the wave angle and the streamwise wave number. The spectrum for a representative configuration is presented in the left part of Fig. 9 where $\lambda^{\parallel} = 0.05$, $\theta = 45^{\circ}$, and Re $= 10000$. The classical branches A, P, and S are present with the unstable mode on the A branch. The shape of the unstable mode is found in the right part of the same figure where the shape of a three-dimensional OS wave can be seen.

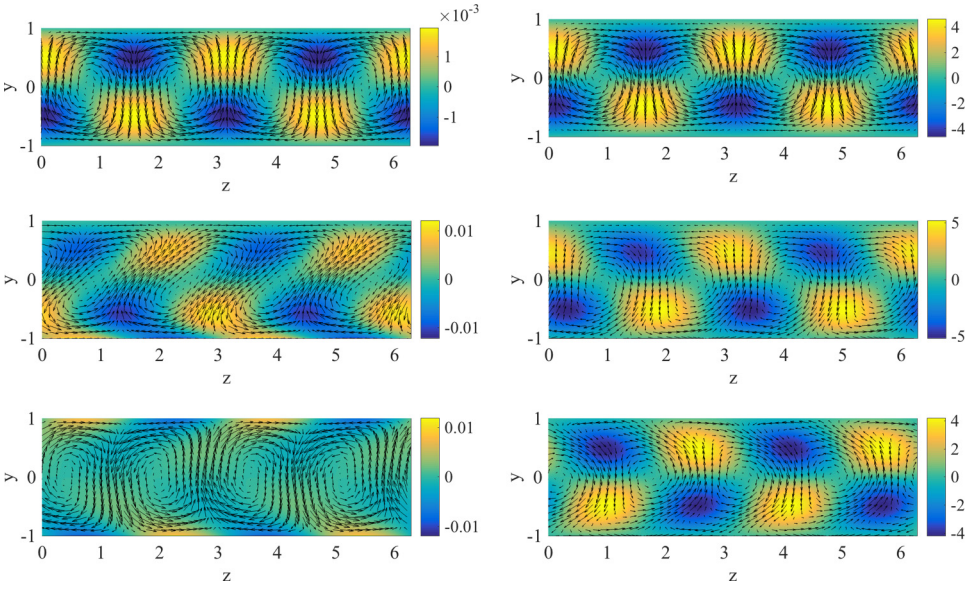

FIG. 10. Vectors and contours, in the (y,z) plane, of the optimal oblique disturbance at $t = 0$ (left column) and at the target time $T = 105$ (right column), shown over two spanwise periods, for $\lambda^{\parallel} = 0$ (top row), $\lambda^{\parallel} = 0.05$ and one SH wall (middle row), $\lambda^{\parallel} = 0.05$, and two SH walls (bottom row). The shaded contours represent the positive and negative streamwise disturbance velocity component, whereas the vectors represent wall-normal and spanwise components. The parameters are Re $= 1333$, $\beta = 2$, $\alpha \approx 0$, $\theta = 30^{\circ}$.

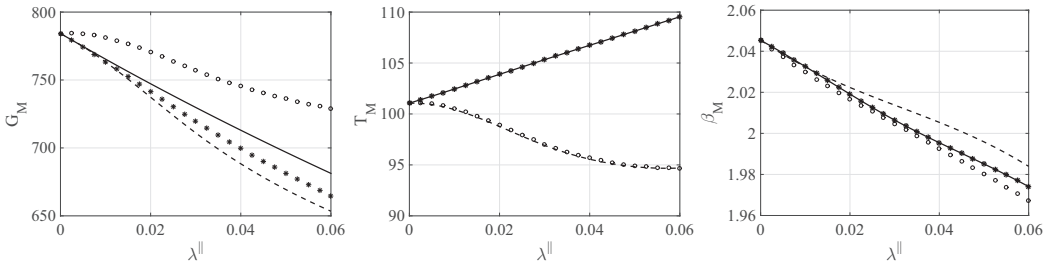

FIG. 11. Gain G_M (left), corresponding time T_M (middle) and spanwise wave number β_M (right) as a function of $\lambda^{\parallel}$ in the case of $\theta = 0^\circ$ $(-)$, $\theta = 15^\circ$ $(*)$, $\theta = 30^\circ$ $(--)$, $\theta = 60^\circ$ $(\circ)$, for $\mathrm{Re} = 1333$ and two SH walls. In all cases the corresponding streamwise wave number is $\alpha_M \approx 0$.

B. Nonmodal analysis

Figure 10 displays representative optimal perturbations (left column) for a given target time, for both no-slip and SH cases, together with their output fields (right column). The intermediate row (one slip wall at $y = -1$) is interesting since the initial disturbance field is more intense near the bottom wall than near the top one and is oblique in the (y,z) plane.

The maximum gain G_M of a disturbance over a given time, maximized with respect to the wave vector, depends parametrically on $\mathrm{Re}, \lambda^{\parallel}$, and θ. The results shown in Figs. 11 through 13 are computed for a fixed value of $\mathrm{Re} = 1333$, which is the same used by Min and Kim [2] (they scaled Re with the centerline velocity yielding a value of 2000). This Reynolds number is subcritical from a modal analysis point of view in the no-slip case.

In Fig. 11 G_M is given as a function of $\lambda^{\parallel}$ for different values of θ, in the case of two SH walls. For $\lambda^{\parallel} = 0$ we recover the no-slip case and for $\lambda^{\parallel} > 0$ there is a monotonic decrease of the gain for all θ. In all cases the corresponding $\alpha_M \approx 0$ and the variation of both β_M and T_M with the slip length is weak. In the case of a single SH wall the results show a different trend, as demonstrated in Fig. 12. Again, the gain G_M is presented as a function of $\lambda^{\parallel}$ for different values of θ. For values of the ridge angle larger than zero the gain always increases as the Navier slip length is increased. Moreover, for some values of the ridge angle θ, and above a threshold $\lambda^{\parallel}$, the flow becomes unstable from a modal point of view: in these cases no finite value of T_M is found, since the gain increases monotonically with the increase of the final target time. An example is presented in Fig. 13, where the gain G is plotted as a function of the final time T of the optimization and three different values of $\lambda^{\parallel}$ for the case in which $\theta = 30^\circ$. With $\lambda^{\parallel} = 0$ and 0.03 the gain decreases for large enough values of T. Conversely, when $\lambda^{\parallel} = 0.06$ the gain increases with T, with the spanwise wave number β

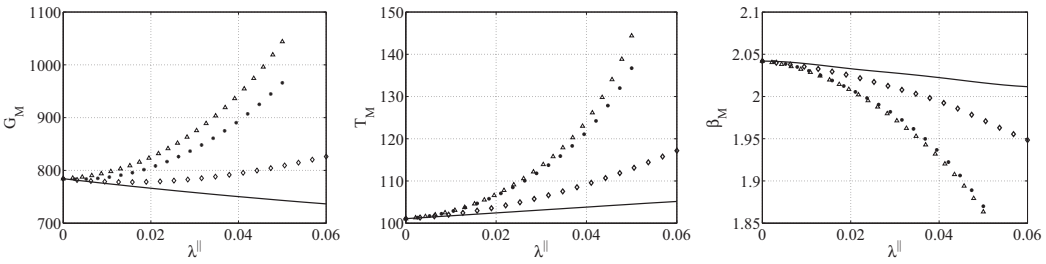

FIG. 12. Gain G_M (left), corresponding time T_M (middle) and spanwise wave number β_M (right) as a function of $\lambda^{\parallel}$ in the case of $\theta = 0^\circ$ $(-)$, $\theta = 15^\circ$ $(\diamondsuit)$, $\theta = 30^\circ$ $(\bullet)$, $\theta = 60^\circ$ $(\triangle)$. In all cases $\mathrm{Re} = 1333$, $\alpha_M \approx 0$, and only one wall is superhydrophobic.

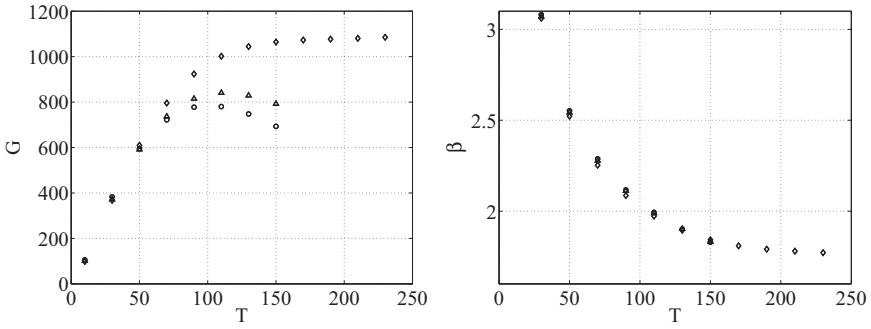

FIG. 13. Gain G (left) and corresponding optimal spanwise wave number β (right) as a function of the final time T, for the case of $\lambda^{\parallel} = 0$ ($\circ$), $\lambda^{\parallel} = 0.03$ ($\triangle$), $\lambda^{\parallel} = 0.06$ ($\Diamond$), $\theta = 30^{\circ}$, $\alpha \approx 0$ and $\mathrm{Re} = 1333$.

reaching an asymptotic value close to 1.78. The unbounded increase of G_M with T is the indication of the occurrence of the streamwise wall-vortex exponential instability.

IV. SUMMARIZING REMARKS

A thorough modal and nonmodal linear stability analysis of the flow in a channel with the walls coated with a SH material has been conducted, for the case of a surface topography constituted by microridges with arbitrary alignment. The main motivation is to understand under which conditions and parameters the most stabilizing or destabilizing effects are obtained. The results obtained give indications on transition delay or enhancement from laminar to turbulent flow and consequently on the possibility of drag reduction.

The modal behavior has yielded surprising results in two senses: On the one hand, a new streamwise wall-vortex mode has been found in the case of a single SH wall, driven by the wall boundary condition, and capable to reduce significantly the value of the Reynolds number for the onset of the instability. This new mode is enhanced by the increase of $\lambda^{\parallel}$ and is found to be most effective when the ridges are inclined by an angle close to 45° to the mean pressure gradient. On the other hand, when two walls are superhydrophobic, the instability is ruled by either a two-dimensional or a three-dimensional Orr-Sommerfeld mode, as function of θ and $\lambda^{\parallel}$, demonstrating *a posteriori* the inapplicability of Squires theorem for this flow.

The nonmodal analysis shows that while the presence of two SH walls yields a slight reduction in energy growth over time, the case of only one SH wall produces an increase of the disturbance kinetic energy for a large range of values of $\lambda^{\parallel}$ when θ is sufficiently greater than zero. It is further shown, in the case of one SH wall, that beyond a threshold slip length, for values of the inclination angle of the microridges around 45°, the gain becomes unbounded with the final target time, a sign of the onset of the wall-vortex instability.

ACKNOWLEDGMENTS

Our activities on SH coatings have started thanks to a gratefully acknowledged *Fincantieri Innovation Challenge* grant, monitored by Cetena S.p.A. (with Giovanni Caprino as program officer).

APPENDIX: WHEN IS THE NAVIER SLIP CONDITION APPLICABLE?

The boundary conditions (2) and (3) used throughout the present analysis for both the base flow, and the perturbations are based on a linearization in the parameters $\lambda^{\parallel}$ and $\lambda^{\perp}$. Inevitably, when the values of $\lambda^{\parallel}$ and $\lambda^{\perp}$ increase the excluded higher order terms are no longer negligible. For applications of the presented method it would be useful to have an estimate of the values of the slip lengths below which we can have some confidence that the Navier slip condition applies.

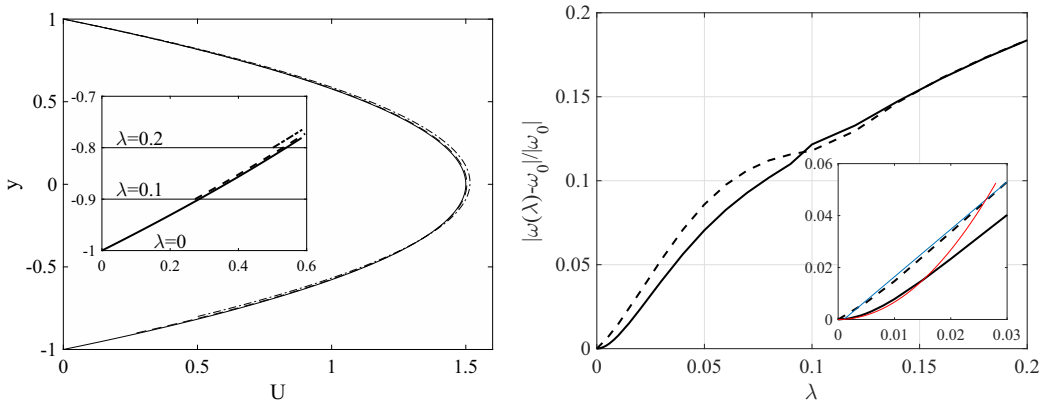

FIG. 14. (Left) Base flow when $\lambda = 0, 0.1, 0.2$; the inset shows a close-up of the lower boundary for three values of $\lambda^{\parallel}$. (Right) Modulus of the difference between the complex frequency ω, for different values of $\lambda^{\parallel}$, and the value of ω when $\lambda^{\parallel} = 0$. Here $\lambda^{\parallel} = \lambda^{\perp}$ (solid line), $\lambda^{\parallel} = 2\lambda^{\perp}$ (dashed line), $\mathrm{Re} = 10\,000$ and $\alpha = \beta = 1/\sqrt{2}$. A linear (blue) and a quadratic (red) functions have been superposed to the results of the two cases to emphasize the behaviors when λ is small (thin lines in the inset).

The error committed by the imposed boundary condition can be evaluated in a manner which has been suggested to us by Paolo Luchini: Let's imagine that we displace the lower wall a distance λ in the vertical direction, from $y = -1$ to $y = -1 + \lambda$ and thus to have slip at the position $y = -1 + \lambda$. The linearized boundary condition (here for the mean flow, but later in the same form also for the perturbation velocity components) at order one is

$$U(-1+\lambda) = \lambda \frac{dU}{dy}(-1+\lambda), \tag{A1}$$

found by assuming no-slip at $y = -1$. The analytical solution of the base flow is simply

$$U(y) = \frac{6}{4-3\lambda^2}\left[1 - y^2 - \frac{1}{2}\lambda^2(1-y)\right], \tag{A2}$$

where we have set $\theta = 0$, for simplicity, which means that $W = 0$. The linearization yields a small nonzero velocity at the lower boundary, $U(-1) = -6\lambda^2/(4-3\lambda^2)$, indicating that the error committed on the mean flow by using Eq. (A1) is of order λ^2. Examples of the base flow profiles are plotted in Fig. 14 (left frame) for three values of λ, demonstrating that small differences appear and increase with the slip length.

The errors in the stability analysis can be evaluated by comparing the complex eigenvalue ω evaluated for different slip lengths against the case for which $\lambda = \lambda^{\parallel} = 0$; a measure of such errors is $|\omega(\lambda^{\parallel}) - \omega(\lambda^{\parallel} = 0)|/|\omega_0|$, with ω_0 the complex angular frequency in Eq. (14) computed for $\lambda = 0$.

Two cases are considered next: one is the case of isotropic roughness, i.e., $\lambda^{\parallel} = \lambda^{\perp} = \lambda$, and the second is the case of longitudinal ridges, for which $\lambda^{\parallel} = 2\lambda^{\perp} = \lambda$. These two cases are expected to yield different behaviors, particularly at low λ, in view of the fact that the only relevant protrusion length scale is the *difference* between $\lambda^{\parallel}$ and $\lambda^{\perp}$. This occurs, as explained by Luchini *et al.* [6], since any physically significant parameter must be independent of the choice of the origin of the wall (which we might for convenience place at the tip of the roughness elements). Thus, it is $\Delta\lambda = \lambda^{\parallel} - \lambda^{\perp}$ which provides a quantitative measure of the effect of roughness on the boundary layer stability behavior; in the case of isotropic roughness $\Delta\lambda = 0$, and the effect must thus be of second order in λ, i.e., the curve of the error must be initially parabolic. Conversely, for longitudinal ridges it is $\Delta\lambda = \lambda^{\parallel}/2$, and the error in the eigenvalue should scale linearly with λ. This is confirmed by our stability calculations (Fig. 14, right frame), carried out at $\mathrm{Re} = 10\,000$ for a disturbance of

wavenumber $k = 1$ inclined by 45° to the x axis, for values of λ up to 0.2. Other inclinations of the perturbation wave yield similar results, confirming the conclusions: in the case of ridges, the linear deviations from the exact solution can be expected to hold until $\lambda \approx 0.05$, whereas the error remains approximately quadratic with λ in the case of cylindrical, regularly spaced posts, only until $\lambda \approx 0.02$. The percentage error in ω remains below 10% for λ up to about 0.1; such a value of the protrusion height could thus be taken as an upper bound, beyond which the Navier slip condition becomes untenable. Some results in the paper obtained for values of λ larger than the threshold above should be considered only as illustrative.

A final note concerns the boundary condition for the normal-to-the wall velocity. Because of continuity, the *homogenized* boundary condition for $\hat{v}$ is simply $\hat{v} = 0$. However, for superhydrophobic walls, with an underformable gas plastron which completely fills the microcavities, it is clearly correct to impose no penetration of the fluid at the tip of the roughness elements, a question might remain when the wetted state is reached: should a protrusion height be defined also for the vertical velocity component? The answer in the case of microridges is no [25], since the solution of the near-wall Stokes problem has only two degrees of freedom, i.e., only two protrusion heights can be defined. Thus, the vanishing of the normal velocity at a given y position rather than another one has only a second order effect on the result, comparable to the error which is made anyway.

[1] A. Bottaro, Superhydrophobic surfaces for drag reduction, Istituto Lombardo (Rend. Scienze) **148**, 239 (2014).
[2] T. Min and J. Kim, Effects of hydrophobic surface on stability and transition, Phys. Fluids **17**, 108106 (2005).
[3] E. Lauga and C. Cossu, A note on the stability of slip channel flows, Phys. Fluids **17**, 088106 (2005).
[4] K. Yu, C. Teo, and B. Khoo, Linear stability of pressure-driven flow over longitudinal superhydrophobic grooves, Phys. Fluids **28**, 022001 (2016).
[5] P. Luchini, in *European Drag Reduction and Flow Control Meeting–EDRFMC 2015, March 23–26, 2015* (University of Cambridge, Cambridge, UK, 2015), pp. 81–82.
[6] P. Luchini, F. Manzo, and A. Pozzi, Resistance of a grooved surface to parallel flow and crossflow, J. Fluid Mech. **228**, 87 (1991).
[7] D. Bechert, M. Bruse, W. Hage, J. Van der Hoeven, and G. Hoppe, Experiments on drag-reducing surfaces and their optimization with an adjustable geometry, J. Fluid Mech. **338**, 59 (1997).
[8] R. García-Mayoral and J. Jiménez, Drag reduction by riblets, Philos. Trans. R. Soc. London A **369**, 1412 (2011).
[9] C. Lee and C.-J. Kim, Maximizing the giant liquid slip on superhydrophobic microstructures by nanostructuring their sidewalls, Langmuir **25**, 12812 (2009).
[10] C. F. Carlborg, G. Stemme, and W. van der Wijngaart, in *IEEE 22nd International Conference on Micro Electro Mechanical Systems, Sorrento, Italy* (IEEE, 2009), pp. 39–42.
[11] C. Lee and C.-J. Kim, Underwater Restoration and Retention of Gases on Superhydrophobic Surfaces for Drag Reduction, Phys. Rev. Lett. **106**, 014502 (2011).
[12] A. Lafuma and D. Quéré, Superhydrophobic states, Nat. Mater. **2**, 457 (2003).
[13] J. R. Philip, Flows satisfying mixed no-slip and no-shear conditions, Z. Andew. Math. Phys. **23**, 353 (1972).
[14] E. Lauga and H. A. Stone, Effective slip in pressure-driven Stokes flow, J. Fluid Mech. **489**, 55 (2003).
[15] M. Z. Bazant and O. I. Vinogradova, Tensorial hydrodynamic slip, J. Fluid Mech. **613**, 125 (2008).
[16] A. V. Belyaev and O. I. Vinogradova, Effective slip in pressure-driven flow past super-hydrophobic stripes, J. Fluid Mech. **652**, 489 (2010).
[17] E. S. Asmolov and O. I. Vinogradova, Effective slip boundary conditions for arbitrary one-dimensional surfaces, J. Fluid Mech. **706**, 108 (2012).
[18] C. Teo and B. Khoo, Flow past superhydrophobic surfaces containing longitudinal grooves: Effects of interface curvature, Microfluidics Nanofluidics **9**, 499 (2010).

[19] H. A. Stone, A. D. Stroock, and A. Ajdari, Engineering flows in small devices. Microfluidics towards Lab-on-a-Chip, Annu. Rev. Fluid Mech. **36**, 381 (2004).
[20] J. Ou and J. P. Rothstein, Direct velocity measurements of the flow past drag-reducing ultrahydrophobic surfaces., Phys. Fluids **17**, 103606 (2005).
[21] P. Schmid and D. Henningson, *Stability and Transition in Shear Flows*, Applied Mathematical Sciences Vol. 142 (Springer, New York, 2001).
[22] J. Szumbarski, Instability of viscous incompressible flow in a channel with transversely corrugated walls, J. Theor. Applied Mech. **45**, 659 (2007).
[23] A. Mohammadi, H. Moradi, and J. Floryan, New instability mode in a grooved channel, J. Fluid Mech. **778**, 691 (2015).
[24] P. Luchini and A. Bottaro, Adjoint equations in stability analysis, Annu. Rev. Fluid Mech. **46**, 493 (2014).
[25] P. Luchini, Linearized no-slip boundary conditions at a rough surface, J. Fluid Mech. **737**, 349 (2013).